Eur. Phys. J. E **25**, 415–424 (2008)
DOI 10.1140/epje/i2007-10308-y

THE EUROPEAN PHYSICAL JOURNAL E

Wetting transitions on textured hydrophilic surfaces

C. Ishino and K. Okumura[a]

Department of physics, Graduate school, Ochanomizu University, Otsuka 2-1-1, Bunkyo-ku, Tokyo 112-8610, Japan

Received 4 December 2007 and Received in final form 5 February 2008
Published online: 23 April 2008 –

Abstract. We consider the quasi-static energy of a drop on a textured hydrophilic surface, with taking the contact angle hysteresis (CAH) into account. We demonstrate how energy varies as the contact state changes from the Cassie state (in which air is trapped at the drop bottom) to the Wenzel state (in which liquid fills the texture at the drop bottom) assuming that the latter state nucleates from the center of the drop bottom. When the textured substrate is hydrophilic enough to allow spontaneous penetration of liquid film of the texture thickness, the present theory asserts that the drop develops into an experimentally observed state in which a drop looks like an egg fried without flipped over (sunny-side up) with a well-defined radius of "the egg yolk." Otherwise, the final contact state of the drop becomes like a Wenzel state, but with the contact circle smaller than the original Wenzel state due to the CAH. We provide simple analytical estimations for the yolk radius of the "sunny-side-up" state and for the final radius of the contact circle of the pseudo-Wenzel state.

PACS. 68.08.Bc Wetting – 68.35.Md Surface thermodynamics, surface energies – 85.40.Hp Lithography, masks and pattern transfer

1 Introduction

Recently, wetting properties of surfaces artificially textured at submicron or nano scales have attracted a considerable attention; the possibility to tune textures to attain desired purposes has been actively explored by experiments, simulations, and theories [1–22]. On such textured surfaces, the contact state of a liquid drop controls the wetting property. Possible contact states include (a) the Cassie state (Fig. 1a) where air is trapped between the bottom of the liquid drop and the solid surface, and (b) the Wenzel state (Fig. 1b) where liquid at the contact penetrates into the texture; the Wenzel drop is very sticky, showing high contact angle hysteresis, while the Cassie drop easily rolls on the surface by small perturbation.

The transition between the Cassie and Wenzel states is theoretically discussed in our previous papers [23,24]. In the first paper [23] we assumed that the transition took place *homogeneously* beneath the contact circle of a drop and explicitly showed the existence of an energy barrier between the two states. In the second paper [24] we proposed transitions taking place *inhomogeneously* by "nucleation" of a small Wenzel patch at the center of the drop bottom: a "nucleus" of radius x created at the center initiates the transition (see Fig. 2a) on a hydrophobic substrate. These two scenarios of homogeneous and inhomogeneous transitions are examined recently through direct observation in [25].

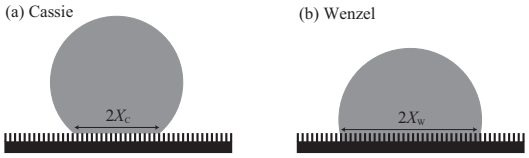

Fig. 1. (a) Cassie drop and (b) Wenzel drop.

Fig. 2. (a) Mushroom state: x is the radius of the "nucleus", and X is the radius of the contact circle. (b) Sunny-side-up state: x is the radius of penetration, and X is the radius of contact circle. X in the sunny-side-up state will be called the yolk radius.

Even on a hydrophilic case, this transition can occur experimentally. As far as we know, however, the main interest in the recent literature has been in the *hydrophobic* case. In particular, *the transition on hydrophilic substrates* has rarely been discussed theoretically except for a few works (*e.g.* a brief discussion in [23]). The main purpose of this paper is to examine the above nucleation scenario in the *hydrophilic* case; as a result we successfully explain

[a] e-mail: okumura@phys.ocha.ac.jp

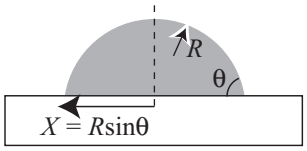

Fig. 3. A drop on a flat or textured surface: R is the radius of curvature of the drop, X is the radius of the contact circle. On the textured surface the angle θ is called *apparent* contact angle because the local contact angle can be inhomogeneous.

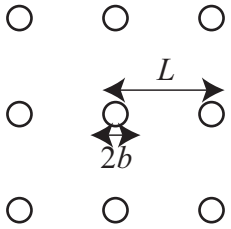

Fig. 4. Top view of the texture.

a recently observed drop state [18,20], termed below as "sunny-side-up state," for the first time; furthermore we provide compact analytical (approximate but precise) expressions (to characterize this state) to be compared with experiments. In addition, the present paper addresses the problem of the contact angle hysteresis, which has been neglected very often in the recent context of wetting on textured surfaces except for a few works [24,26,27].

Let us consider a reference state composed of spherical drop (radius R_0) and a flat surface (surface energy γ_S). If we put the drop on the surface, the shape of the drop is like a spherical cap with the contact angle θ and radius R (Fig. 3). Because the volumes of the above two drops are the same, the following relationship between R and R_0 holds:

$$R/R_0 = 2^{2/3}(2 - 3\cos\theta + \cos^3\theta)^{-1/3}. \tag{1}$$

With use of this R, the surface area of the spherical cap is given by

$$S_C(\theta) = 2\pi R^2(1 - \cos\theta). \tag{2}$$

The bottom radius of the drop on the surface in Figure 3 is defined here as

$$X = R\sin\theta, \tag{3}$$

from which the bottom area is given by

$$S_B(\theta) = \pi R^2 \sin^2\theta \ (= \pi X^2). \tag{4}$$

With the aid of S_C and S_B, given above, the surface energy of the drop is given by [23,24]

$$E = \gamma S_C(\theta_E) - \gamma\cos\theta_E S_B(\theta_E), \tag{5}$$

where we have used Young's equation with θ_E the equilibrium contact angle on the flat substrate:

$$\gamma\cos\theta_E = \gamma_S - \gamma_{SL}. \tag{6}$$

In equation (5), $-\gamma\cos\theta_E = \gamma_{SL} - \gamma_S$ corresponds to *the energy of replacement* per unit area of the solid (dry) surface (described by the surface energy γ_S) with the solid-liquid (wet) surface (γ_{SL}).

If we put a drop on a non-flat textured surface, the energy of a drop changes. We consider a model surface textured by a forest of cylindrical pillars arranged in a square lattice with lattice constant L where the radius and height of the pillars are b and h, respectively, as in Figure 4. The surface roughness r is given as the ratio of the actual area to the projected area: $r = 1 + 2\pi bh/L^2$. The solid fraction ϕ of the contact circle at the bottom of the Cassie drop can be represented by $\phi = \pi b^2/L^2$.

In the case of Cassie drop (Fig. 1a), the contact angle is given by *the average of contact angles on the solid and "air" substrates* (the latter angle can be regarded as π so that its cosine is -1) [28]:

$$\cos\theta_C = \phi\cos\theta_E - (1 - \phi), \tag{7}$$

and the surface energy becomes [23,24]

$$E_C = \gamma S_C(\theta_C) - \gamma\cos\theta_C S_B(\theta_C). \tag{8}$$

Here, as in equation (5), $-\gamma\cos\theta_C$ corresponds to *the energy of replacement* per unit area of the solid (dry) textured surface with the wetting state of Cassie.

Similarly, because the apparent contact angle of the Wenzel drop (Fig. 1b) is determined as

$$\cos\theta_W = r\cos\theta_E, \tag{9}$$

the surface energy is expressed as [23,24]

$$E_W = \gamma S_C(\theta_W) - \gamma\cos\theta_W S_B(\theta_W). \tag{10}$$

Here, $\gamma\cos\theta_W$ corresponds to *the energy of replacement* per unit area of the solid (dry) textured surface with the wetting state of Wenzel. Note that, *the value of* $r\cos\theta$ *in equation* (9) *can exceed one*. Even in such a case, we will call this quantity $\cos\theta_W$ as in equation (9) for convenience. We emphasize here that equations (8) and (10) can be regarded as natural extension of equation (5) [23,24].

2 Drop energies of intermediate states

In our previous work [24] we characterized the intermediate states during the transition from the Cassie to Wenzel state by two variables x and X (see Fig. 2) and calculated the steepest-descent path in the energy landscape shown on the (x, X)-plane in order to determine how the intermediate states (*i.e.*, x and X) change during the transition: we demonstrated a scenario that nucleation occurs during the transition from the Cassie state to the Wenzel state with the liquid penetrating into the texture from the center. In this previous work mainly for hydrophobic cases, other than the conventional Wenzel and Cassie states, novel characteristic states emerged in the theory, called the pseudo-Wenzel state and the mushroom state.

In the present work mainly for hydrophilic cases, still another representative state emerges as we see below. We

call this a "sunny-side-up" state, which was recently observed (see Fig. 7 of Ref. [18]).

The above three non-conventional states are characterized as follows:

- "Mushroom" state (Fig. 2a): the penetration front represented by x is inside of the (macroscopic) contact circle (radius X). Here, x is the radius of "nucleus" ($x < X$).
- Pseudo-Wenzel state: the penetration front coincides with the contact circle (radius X). This state is similar to the Wenzel state (Fig. 1b) but the contact circle radius X is different from that of the Wenzel state ($x = X$).
- "Sunny-side-up" state (Fig. 2b): the penetration front is outside of the contact circle ($x > X$). X in this state is called the yolk radius.

Below we investigate the surface and hysteresis energy as a function of x and X and show that these non-conventional states can appear in practice as characteristic states.

Note that a deposited drop can realize the Cassie state even on a hydrophilic surface; in such a case, the wetting state can be changed into the Wenzel state by external perturbation, say by pushing the drop. For such transitions, an initial barrier of the order of $\gamma(L^2+4Lh)$ should be overcome first to establish the smallest Wenzel patch at the drop bottom. This initial barrier, which can be enhanced by the contact angle hysteresis in practice, is much larger than the thermal energy and can be larger than the gravitational or vibrational energy of a millimeter drop when gently put on the surface, which vindicates the observation of the Cassie state even on the hydrophilic substrate. In the following calculation, we assume that the drop already conquers this initial barrier to establish a tiny Wenzel patch or nucleus of radius x, with x being small but larger than the texture scale.

2.1 Without contact angle hysteresis

In this subsection, we derive the surface energy of a drop for given x (nucleus size) and X (drop bottom radius), neglecting contact angle hysteresis (both in hydrophobic and hydrophilic cases for completeness). We first determine R and the *apparent* contact angle θ in Figure 3 *on a non-flat textured surface* for a given X. From equation (3), θ $(=\theta_X)$ is obtained once X is given:

$$\cos\theta_X = \begin{cases} (1-(X/R_X)^2)^{1/2}, & \text{for } \theta_X < 90^\circ, \\ -(1-(X/R_X)^2)^{1/2}, & \text{for } \theta_X > 90^\circ, \end{cases} \tag{11}$$

where $R = R_X$ can be specified by equation (1) with this $\theta = \theta_X$, *i.e.*, R_X is obtained as a solution of the nonlinear equation,

$$4(R_0/R_X)^3 = 2 \pm 3(1-(X/R_X)^2)^{1/2} \mp (1-(X/R_X)^2)^{3/2}, \tag{12}$$

where the top and bottom signs should be used in "hydrophilic" cases ($\theta_X < 90^\circ$) and in "hydrophobic" cases ($\theta_X > 90^\circ$), respectively.

In this situation, since R and θ are specified once X is given, S_C and S_B determined by R and θ as in equations (2) and (4) are given as functions of X (while S_C and S_B are given once θ is given in equations (5), (8) and (10)). To emphasize this, we use the notation $S_C(X)$ and $S_B(X)$ in the following.

In the case of $x < X$ (*i.e.*, mushroom state in Fig. 2a), we obtain the surface energy

$$E(x,X) = \gamma S_C(X) + \gamma(1-\phi)\pi(X^2-x^2) + (\gamma_{SL}-\gamma_S)\phi\pi X^2 + (\gamma_{SL}-\gamma_S)(r-\phi)\pi x^2. \tag{13}$$

The first and second terms are the energy associated with the liquid-air interface γ for the cap of the drop and the doughnut area at the drop bottom. The third and forth terms are the energy associated with the replacement of the dry solid surface γ_S by the wet solid surface γ_{SL}. Using equation (6), the above energy can be cast into the following form:

$$E(x,X)/\gamma = S_C(X) - \{f_W\cos\theta_W + (1-f_W)\cos\theta_C\}S_B(X), \tag{14}$$

where

$$f_W = x^2/X^2. \tag{15}$$

Recall here that $\cos\theta_W$ is a quantity defined by equation (9), which can exceed one. In equation (14), γ times the quantity in the curly bracket corresponds to the energy of the replacement per unit area of the solid (dry) surface with the wetting state comprised of the Wenzel and the Cassie states.

Equation (14) gives the drop energy as a function of x and X for a given texture (*i.e.*, for fixed ϕ and r). This equation (14) can be regarded as a natural extension of equations (8) and (10): we recover equation (8) when $f_W = 0$ while recover equation (10) when $f_W = 1$.

In the case of $x \geq X$ (*i.e.*, sunny-side-up state in Fig. 2b), we have

$$E(x,X) = \gamma S_C(X) + (\gamma_{SL}-\gamma_S)rS_B(X) + \pi(x^2-X^2)\{(\gamma_{SL}-\gamma_S)(r-\phi)+\gamma(1-\phi)\}, \tag{16}$$

where the first term corresponds to the surface energy of the drop cap, the second to that of the solid-liquid contact at the bottom, and the third to that of doughnut area which concerns both the solid-liquid contact and the liquid-air contact (the top surface of pillars is assumed dry because γ_S (dry state) is always smaller than $\gamma+\gamma_{SL}$ (wet state)). Using equation (6) we can again express the energy as a function of x and X:

$$E(x,X)/\gamma = S_C(X) - \{f_W\cos\theta_W + (1-f_W)\cos\overline{\theta}_C\}S_B(X), \tag{17}$$

Table 1. Parameters used in our calculation: θ_E is the contact angle on a flat surface, b and h are pillar radius and pillar height, respectively, in the unit where the pillar distance L is 10, *i.e.*, L is fixed in our calculations. If we assume that L is $10\,\mu$m, it amounts to that b and h in this table are given in the unit of micron.

	θ_E	b	h	ϕ	r	α
A	45	1.5	3	0.071	1.3	−0.072
B	60	1.5	6	0.071	1.6	−0.18
C	45	1.5	6	0.071	1.6	0.13
D	60	1.5	12	0.071	2.1	0.10

where $\overline{\theta}_C$ is *the average of contact angles on the solid and "liquid" substrates* (the latter angle can be regarded as 0 so that its cosine is 1),

$$\cos\overline{\theta}_C = \phi\cos\theta_E + (1-\phi). \tag{18}$$

In equation (17), γ times the quantity in the curly bracket corresponds to the energy of the replacement per unit area of the solid (dry) surface with the wetting state comprised of the Wenzel state and the wetting film of thickness h.

Equations (14) and (17) can be written in a unified form, using equations (2) and (4):

$$E(x,X)/\gamma = S_C(X) - \cos\theta^* S_B(X) - \pi\alpha^* x^2, \tag{19}$$

where

$$\alpha^* = \cos\theta_W - \cos\theta^*, \tag{20}$$

$$\cos\theta^* = \begin{cases} \cos\theta_C, & x \le X, \\ \cos\overline{\theta}_C, & x \ge X. \end{cases} \tag{21}$$

For later convenience, we express this in a dimensionless form:

$$\varepsilon(x,X) \equiv E(x,X)/E_0 = \left(\frac{2}{1+\cos\theta_X} - \cos\theta^*\right)\overline{X}^2 - \alpha^*\overline{x}^2, \tag{22}$$

with the following definitions:

$$E_0 = \pi\gamma R_0^2, \tag{23}$$

$$\overline{X} = X/R_0, \tag{24}$$

$$\overline{x} = x/R_0. \tag{25}$$

Note that this expression is valid both for "hydrophilic" and for "hydrophobic" cases, together with equations (11) and (12).

To draw physical scenarios from the energy expression in particular in hydrophilic cases (see [24] for hydrophobic cases), we first present some numerical behaviors of equation (19) and later consider some analytical properties. We used the typical parameter set A-D specified in Table 1.

These parameters are selected so that they include two distinct regimes of penetration and non-penetration. These regimes are distinguished by the sign of the coefficient of x^2 in equation (19) for $x \ge X$. If it is positive, the surface energy E becomes smaller as x increases and the penetrating area becomes larger. The positive condition, or *the penetration condition* is given by

$$\cos\theta_E > \frac{1-\phi}{r-\phi}, \tag{26}$$

or, equivalently by $\alpha > 0$ with the definition of *a penetration strength*

$$\alpha = \cos\theta_W - \cos\overline{\theta}_C. \tag{27}$$

Indeed, $\gamma\alpha$ corresponds to the energy of replacement per unit area of the Wenzel state with the wetting film. If the Wenzel angle θ_W is smaller than the average $\overline{\theta}_C$ of the contact angles on the solid and "liquid" substrates, penetration of liquid film proceeds into texture on hydrophilic substrates (this picture is valid so long as $\cos\theta_W$ does not exceed one). In Figure 5, the (b,h)-plane is divided into two regimes according to equation (26) where the upper side of the curve corresponds to the penetration regime ($\alpha > 0$).

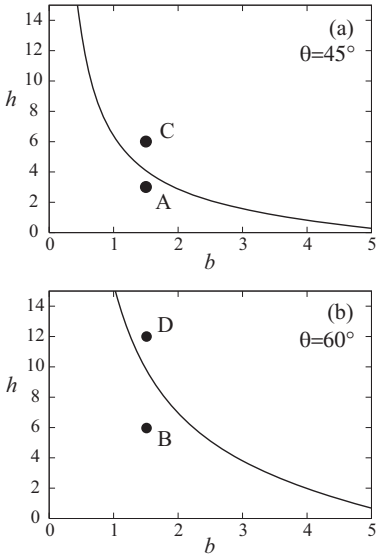

Fig. 5. The penetration condition on the (b,h)-plane for $L = 10\,\mu$m. (a) Contact angle is 45°, (b) contact angle is 60°, where the units of b and h are both micron (or they are in arbitary units so long as b, h and L are in the same unit and much smaller than the drop size).

In Figure 6, we present numerical estimations of the energy in the hydrophilic case in equation (19) on the (x,X)-plane, with using the parameter set A-D, specified in Table 1. These are contour plots of three-dimensional plots, one example of which is shown in Figure 7. In numerical calculations, we first find the root of equation (12) and then use equation (11) to calculate equation (19).

The 3D landscape in Figure 7 of the corresponding contour plot in Figure 6A predicts a scenario (a) → (b) → (c) → (d1) → (e1) illustrated in Figure 8. This can be understood as follows: the solid curve in Figure 6A or Figure 7 represents the steepest-descent line, which starts from the Cassie state (Fig. 8a) located at the point P_C ($x = 0, X = X_C$), ending up with the Wenzel state

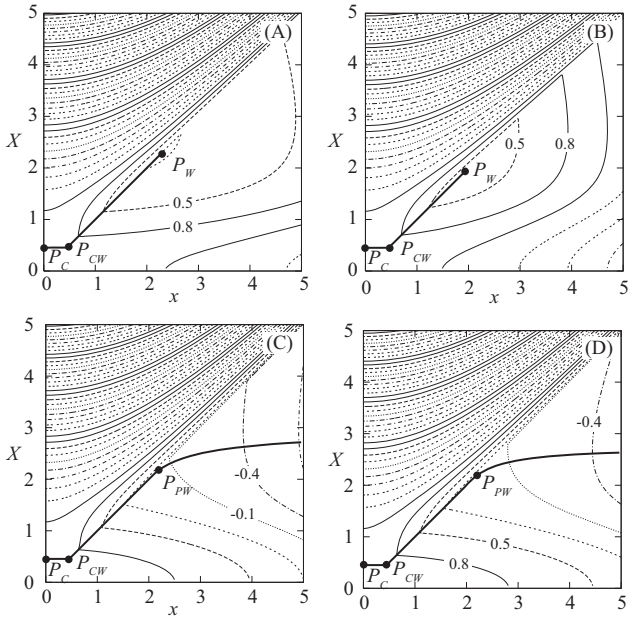

Fig. 6. Contour plots of energy given in equation (19) for parameter sets A, B, C, D, without CAH. The unit length for x and X is R_0 while that of energy is $4\pi\gamma R_0^2$. A and B are in the non-penetrating regime ($\alpha < 0$), while C and D are in the penetrating regime ($\alpha > 0$).

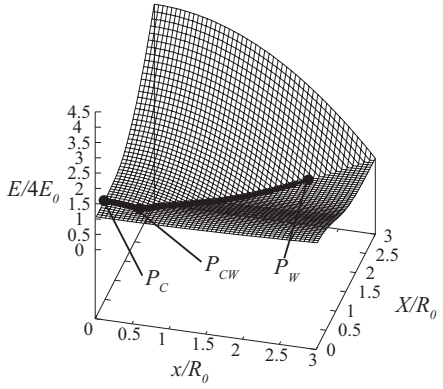

Fig. 7. Three-dimensional plot of the surface energy for the parameter set A, without CAH, which corresponds to Figure 6A.

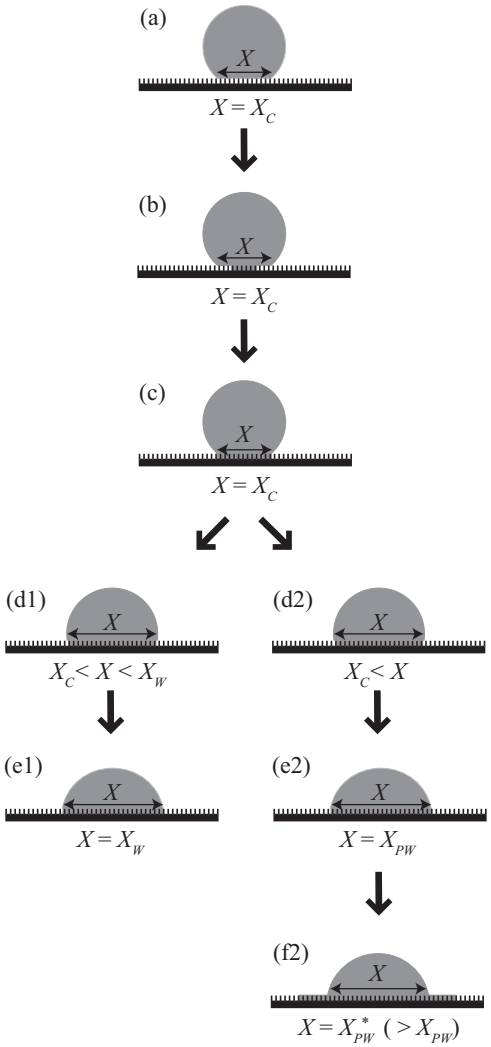

Fig. 8. Transition from the Cassie state to the Wenzel state in the non-penetration regime defined by $\alpha < 0$ (left) or sunny-side-up state in the penetration regime defined by $\alpha > 0$ (right). (a) Cassie state, (b) mushroom state, (c) pseudo-Wenzel state at $X = X_C$, (d1) pseudo-Wenzel state at X with $X_C < X < X_W$, (d2) pseudo-Wenzel state (at $X > X_C$), (e1) Wenzel state, (f2) sunny-side-up state. When CAH comes into play, the left scenario is realized both in the non-penetration regime ($\alpha < 0$) and in the weak penetration regime ($0 < \alpha < \Delta$) in which the size of X in the final state (e1) gets smaller due to the CAH, while the right scenario is realized in the strong penetration regime ($\alpha > \Delta$) in which the initial yolk size X_{PW} in (e2) and the final size X_{PW}^* in (f2) get larger and smaller, respectively, due to the CAH.

(Fig. 8e1) at P_W ($x = X = X_W$), via P_{CW} (corresponding to Fig. 8c). Note that i) between P_C and P_{CW} only x increases while X is fixed (Fig. 8b) and ii) between P_{CW} and P_W both x and X simultaneously increase and always coincide with each other (Fig. 8d1). The same story, (a) → (b) → (c) → (d1) → (e1) in Figure 8, applies also for Figure 6B.

Similar to Figure 6A and B ($\alpha < 0$), in Figure 6C and D ($\alpha > 0$), the starting point is P_C and it moves down to P_{CW}, following the steepest-descent path. From P_{CW}, a pseudo-Wenzel drop enlarges the bottom area or X (Fig. 8d2) with keeping $x = X$ until the drop arrives at P_{PW} (Fig. 8e2), where $X = X_{PW}$. Then, differently from Figure 6A and B, the drop starts to make a "sunny-side up" (Fig. 8f2) and the penetrating size x expands with *the egg yolk radius* X gradually increasing from an initial value X_{PW} to a maximum value X_{PW}^* where the *initial and final yolk radii* X_{PW} and X_{PW}^* are different form X_W (in Fig. 6C and D, the literal Wenzel angle is 0°, where X_W is interpreted as an infinity).

The reason why X is fixed to X_C during the transition from P_C to P_{CW} is clear from equation (19): this equation states that, in the region $X > x$, the energy is the minimum when the apparent contact angle is the Cassie

angle θ_C, *i.e.*, when $X = X_C$, if we neglect the last term $(\alpha^* x^2)$.

The final radius X^*_{PW} can be determined also from equation (19), which asserts that, for $x < X$, the energy is the minimum when the apparent contact angle is $\overline{\theta}_C$ if we neglect the $\alpha^* x^2$ term: the final yolk size X^*_{PW} is given by the radius when the angle is $\overline{\theta}_C$, *i.e.*, the average of the angles θ_E on the solid and 0 on the "liquid." Later, we discuss this final radius X^*_{PW} together with the initial radius X_{PW} in more details, because these quantities can be measured in future experiments.

In summary, in the non-penetration regime ($\alpha < 0$) as in Figure 6A and B, the final state of the drop is the Wenzel state (Fig. 8e1) while X is fixed to the initial Cassie value X_C until x catches up to this X_C and then x expands with keeping $x = X$ to the final value X_W. In the opposite case of penetrating regime ($\alpha > 0$) as in Figure 6C and D, the transition proceeds in a way similar to that in the non-penetration regime but, after the expansion process of x with keeping $x = X$ to reach $x = X = X_{PW}$, the drop starts to make the "sunny-side up" (Fig. 8f2) and x continues to expand with the yolk size gradually increasing from X_{PW} to X^*_{PW}. The final yolk radius is that when the angle is $\overline{\theta}_C$ (the present theory is valid so long as the volume of the penetrating film is negligible to the drop volume).

2.2 Hysteresis energy

Let us imagine that a liquid drop is deposited on a "flat" surface, and that liquid is added to the drop by a pipet. At first, the contact line does not move while the contact angle increases: when the contact angle exceeds a critical angle θ_A, the contact line suddenly advances. This pinning occurs even on a "flat" surface which has usually defects on it. We call the critical value θ_A the advancing angle [28]. This implies that when the contact line is adiabatically moving at the advancing angle θ_A the contact line is dragged by a force f_d per unit length determined by the force balance in the horizontal direction in Figure 9: $f_d + \gamma_{SL} + \gamma \cos\theta_A = \gamma_S$.

Here, a contact angle hysteresis (CAH) is measured by δ or $\delta\theta$ defined as follows:

$$\delta = |\cos\theta_A - \cos\theta_E|, \tag{28}$$

$$\delta\theta = \theta_A - \theta_E. \tag{29}$$

With this δ the drag force f_d working on a contact line is expressed as $\gamma\delta$ per unit length of the line. This implies an extra energy $f_d l d = \gamma\delta A$ to move a contact line of length l by a distance d with the swept area $A = ld$.

We have two important types of hysteresis on textured surfaces. One is from the friction created when the contact line moves on the side of the cylindrical pillars as illustrated in Figure 10a. The other is from the friction occurring when the contact line moves on the bottom surface of the substrate on which the pillars are built as in Figure 10b.

The surface area of the side of a pillar is written as $2\pi bh$, while the contact line passes through $\pi x^2/l^2$ pillars

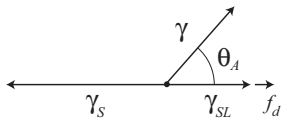

Fig. 9. The force balance at the contact line moving adiabatically when the contact angle is equal to the advancing angle.

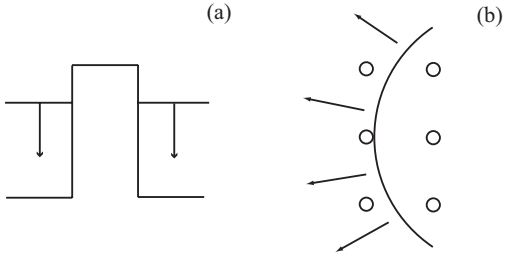

Fig. 10. Two representative modes of CAH. (a) The hysteresis associated with the wall of the pillar. (b) The hysteresis associated with the bottom surface of the substrate on which the pillars are built.

till the radius of the bottom of a drop reaches x. Thus, the first hysteresis energy from the side area can be estimated as

$$E_p = (r-1)\,\pi\gamma\delta x^2. \tag{30}$$

On the contrary, the second hysteresis energy from the bottom surface, $\pi x^2(1-\phi)$, is given by

$$E_b = (1-\phi)\pi\gamma\delta x^2. \tag{31}$$

There could be a third contribution associated with the friction occurring when the contact line moves on the top surface of the pillars, which would contribute if there were processes in which X increased in the mushroom state ($X > x$); since the steepest-descent path without CAH does not include such processes, this pillar surface contribution is not considered below.

Consequently, the total energy coming from the surface and the hysteresis energy is given by $E_A = E + E_p + E_b$, or

$$E_A/\gamma = S_C(X) - \cos\theta^* S_B(X) - \pi\,(\alpha^* - \Delta)\,x^2, \tag{32}$$

with

$$\Delta = (r-\phi)\,\delta. \tag{33}$$

Figure 11 shows the contour plots of the energies with the hysteresis given in equation (32) on the (x, X)-plane when the contact angle hysteresis (CAH) $\delta\theta$ is either 5° (A1-D1) or 20° (A2-D2). The parameter sets A-D used for Figure 11 are those given in Table 1 as before: A1, A2, B1, and B2 are in the non-penetration regime ($\alpha < 0$), while C1, C2, D1, and D2 are in the penetration regime ($\alpha > 0$).

As seen in Figure 11A1, A2, B1, and B2, when the penetration condition, $\alpha > 0$, is not satisfied, the final state always becomes the pseudo-Wenzel state, with the final size X_{PW} different from X_W. Even when this condition is satisfied, the final state could become the pseudo-Wenzel state if the CAH is large (see Fig. 11C2, D1, and D2). However when the CAH is small, in the final phase

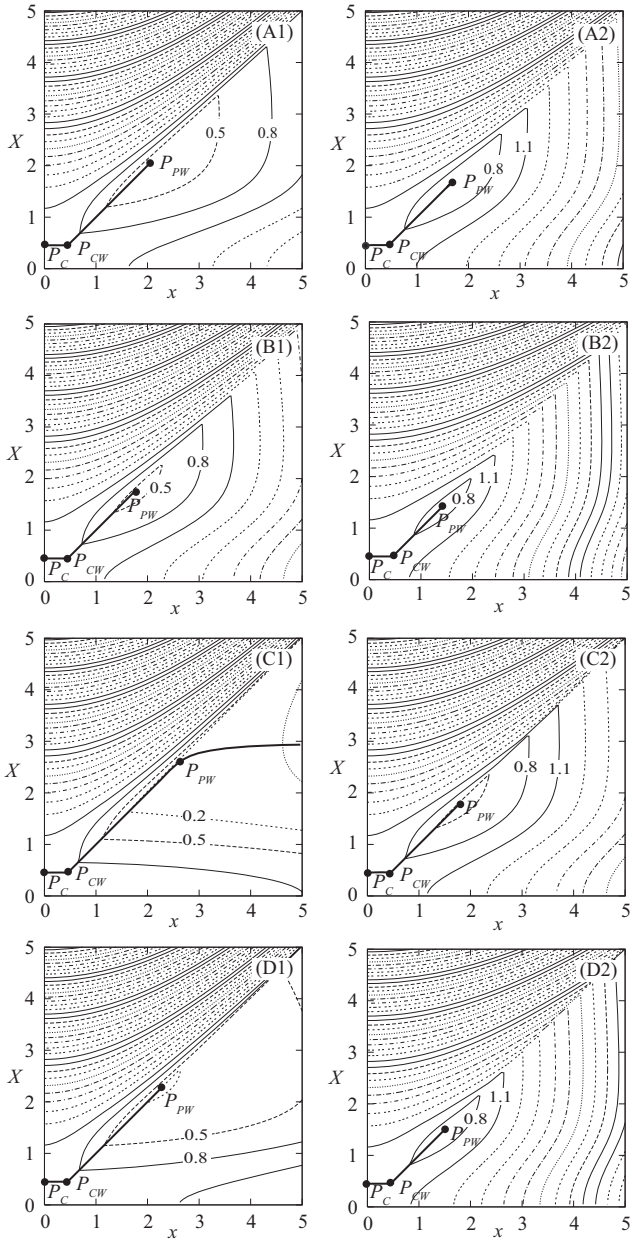

Fig. 11. Contour plots of energy given in equation (32) for parameter sets A, B, C, D, with CAH. CAH of A1-D1 and A2-D2 are 5 and 20 degrees, respectively. The unit length for x and X is R_0 while that of energy is $4\pi\gamma R_0^2$, as in Figure 6. A and B are in the non-penetration regime ($\alpha < 0$), while C and D are in the weak penetration regime ($0 < \alpha < \Delta$) except C1; C1 is in the strong penetration regime ($\alpha > \Delta$).

of sunny-side up, x keeps increasing with X gradually increasing from the initial yolk radius X_{PW} to the final yolk radius X^*_{PW} (see Fig. 11C1): an "egg white" film of height h advances with a well defined "yolk" (as long as the film volume is much smaller than the liquid drop). As mentioned before, this is consistent with experiments (Fig. 7 in [18]).

When the final state becomes the pseudo-Wenzel state, the bottom radius ($x = X$) of the final state becomes smaller as the CAH increases. Namely the apparent contact angle becomes larger (*e.g.*, compare Fig. 11A1 with A2).

When the sunny-side-up state "survives" the hysteresis (Fig. 11C1), the final yolk radius X^*_{PW} is the same as that in cases without hysteresis as seen from equation (32) because this equation is the same as equation (19) except that the coefficient α^* is replaced with $\alpha^* - \Delta$. Equation (32) requires the condition for the penetration:

$$\alpha > \Delta \tag{34}$$

i.e., the penetration strength should be stronger than the hysteresis effect Δ for the penetration. This condition will be confirmed again in a different context below. See also the caption of Figure 8 for a summary with illustration.

3 Small contact angle approximation

In this section, we derive useful analytical formulae, *e.g.* a formula for the yolk radius in the penetration regime, when the *apparent* contact angle θ is relatively small, *i.e.*, when the contact circle X is large.

Without making this small θ approximation, we explicitly have the final yolk size,

$$X^*_{PW} = 2^{2/3}(2 - 3\cos\overline{\theta}_C + \cos^3\overline{\theta}_C)^{-1/3}\sin\overline{\theta}_C, \tag{35}$$

regardless of the existence of the CAH. If we calculate this for Figures 6C and D, we have $X^*_{PW} = 2.96$ and 2.71, respectively. This suggests that, in Figure 6C in particular, the yolk size keeps increasing as x increases further; indeed, in Figure 11C1, for which X^*_{PW} is the same as that in Figure 6C, X^*_{PW} approaches 2.96 at smaller values of x.

As seen above, in general, the convergence of the yolk size from the initial value X_{PW} to the final value X^*_{PW} can be slow. Thus, it is worthwhile giving an estimate for the onset value X_{PW} for experimental confirmation of the current theory. This estimate is tractable when θ is small as shown from now on.

When $\theta \ll 1$ or $X \gg R_0$, we obtain $R = (3\theta^4/16)^{-1/3}$ from equation (1), which gives $\theta = 16/(3\overline{X}^3)$ from equation (3). This expression allows us an approximate final yolk size

$$X^*_{PW} = \left(\frac{16}{3\overline{\theta}_C}\right)^{1/3} R_0. \tag{36}$$

This formula gives $X^*_{PW} = 2.97$ and 2.71 for the parameter sets C and D, respectively; the values are indistinguishable from the ones obtained from the exact formula in equation (35) even though θ_E ($= \pi/4$ or $\pi/3$) is not very small.

In a similar manner we obtain for $\overline{X}^3 \gg 16/3$ (*i.e.*, $X > R_0$)

$$\varepsilon(x, X) = \frac{c}{\overline{X}^4} - \beta\overline{X}^2 - \alpha\left(\overline{x}^2 - \overline{X}^2\right), \tag{37}$$

where

$$\beta = \cos\theta_W - 1, \tag{38}$$

$$c = (8/3)^2. \tag{39}$$

This formula can reproduce the energy landscape easily without the numerical root-finding for $X > R_0$. A similar approximation is possible also for θ around $\pi/2$ and π, equivalently, for X around R_0 and 0.

The steepest-descent direction on the (x, X)-plane in the region $x > X$ is given by a unit vector

$$(n_x, n_y) = \frac{(-\varepsilon_x, -\varepsilon_X)}{\sqrt{\varepsilon_x^2 + \varepsilon_X^2}}, \tag{40}$$

where

$$\varepsilon_x = \frac{\partial\varepsilon}{\partial\overline{x}} = -2\alpha\overline{x}, \tag{41}$$

$$\varepsilon_X = \frac{\partial\varepsilon}{\partial\overline{X}} = 2(\alpha-\beta)\overline{X} - \frac{4c}{\overline{X}^5}, \tag{42}$$

because $\nabla[z-\varepsilon(x,X)]$ is normal to the surface $z = \varepsilon(x,X)$ in the (x, X, z) coordinate system. The variation $\mathrm{d}s$ in this direction corresponds to variations $\mathrm{d}x = n_x\mathrm{d}s$ and $\mathrm{d}X = n_y\mathrm{d}s$ in the x and X directions, respectively. The gradient of ε along this direction is thus given by

$$\frac{\mathrm{d}\varepsilon}{\mathrm{d}s} = \frac{\partial\varepsilon}{\partial x}\frac{\mathrm{d}x}{\mathrm{d}s} + \frac{\partial\varepsilon}{\partial X}\frac{\mathrm{d}X}{\mathrm{d}s} \tag{43}$$

$$= -\sqrt{\varepsilon_x^2 + \varepsilon_X^2}. \tag{44}$$

In the limit of $x \to X$ with $x > X$, the gradient is expressed as

$$G_1 = -\sqrt{(2\alpha\overline{X})^2 + \left[2(\alpha-\beta)\overline{X} - 4c/\overline{X}^5\right]^2}, \tag{45}$$

with α defined in equation (27).

The gradient of ε along the line $x = X$ is given by $G_2 = (\partial\varepsilon/\partial\overline{x}')_{\overline{X}'=0}$, where the $(\overline{x}', \overline{X}')$ coordinate system is the one obtained by the rotation of the $(\overline{x}, \overline{X})$ coordinate system around the origin by 45 degrees; the right-hand side is the partial derivative with respect to $\overline{x}'$ with ε as a function of $\overline{x}'$ and $\overline{X}'$ evaluated at $\overline{X}' = 0$, *i.e.*, at $x = X$. This quantity can be calculated as

$$G_2 = -\frac{1}{\sqrt{2}}\left(\frac{4c}{\overline{X}^5} + 2\beta\overline{X}\right) < 0. \tag{46}$$

The *initial* yolk radius can be defined as a point on the (x, X)-plane on the steepest-descent path where the descent direction deviates from the line $x = X$ as mentioned above. In other words, *the initial radius of the yolk X_{PW} is given as the solution of the equation*

$$G_1 = G_2. \tag{47}$$

This equation can be explicitly solved. The solution is given by

$$X_{PW} = \left(\frac{2c}{2\alpha-\beta}\right)^{1/6} R_0. \tag{48}$$

The numerical values given from this for Figures 6C and D are $X^*_{PW} = 2.13$ and 2.17, respectively, which reproduce the values indicated in the plots, although θ_E is fairly large or close to one ($\theta_E = \pi/4$ or $\pi/3$).

Extension to the case with CAH is trivial and the initial yolk radius in equation (48) can be replaced with a generalized expression

$$X_{PW} = \left(\frac{2c}{2\alpha-\beta-\Delta}\right)^{1/6} R_0, \tag{49}$$

with Δ defined in equation (33). This formula gives $X_{PW} = 2.55$ for Figure 11C1, which is again almost precise as seen in the plot. This equation (49) predicts that an increase in Δ enlarges the initial yolk radius (compare, for example, Fig. 6C with Fig. 11C1).

We can also derive the expression for the radius of contact circle for the final Wenzel or pseudo-Wenzel state in the non-penetrating regime from the condition $G_2 = 0$:

$$X_{PW} = \left(\frac{2c}{\Delta-\beta}\right)^{1/6} R_0. \tag{50}$$

This radius at $\Delta = 0$ gives an approximate radius in the Wenzel state. Note that $-\beta$ is positive in the non-penetrating regime ($\alpha < 0$) (see Eq. (51) below). This expression is also valid in the penetration regime when $\Delta - \beta$ is positive. In such a case, this equation (50) gives the final radius of the contact circle of a drop which fails to develop into the sunny-side-up state. In both cases, from equation (50), the final pseudo-Wenzel size X_{PW} is predicted to decrease as the hysteresis Δ increases (compare, for example, Fig. 11D1 with D2).

Equation (50) also gives good numerical estimates. The final pseudo-Wenzel radii X_{PW} specified by the point P_{PW}, in Figure 11A1 in the non-penetrating regime ($\alpha < 0$) and in Figure 11C2 in the penetrating regime ($\alpha > 0$), calculated from equation (50) are 2.09 and 1.88, respectively, which agree well the values indicated in the plots.

Within the above approximation, we can derive the condition for the sunny-side-up state to be realized in the penetration regime when $\Delta \neq 0$. This condition amounts to that the initial yolk size in equation (49) is smaller than the size given in equation (50), which recovers equation (34), *i.e.*, $\alpha > 0$, as announced. This condition, $\alpha > 0$, defines *the strong penetration regime*. The physical meaning of this condition is clear: when the penetration strength α exceeds the effect of CAH, the sunny-side-up state is realized. Otherwise, *i.e.*, *in the weak penetration regime* ($0 < \alpha < \Delta$) or *in the non-penetration regime* ($\alpha < 0$), the drop gets trapped into a (pseudo-) Wenzel state. Note that *the strong penetration condition* ($\alpha > \Delta$) guarantees the positivity of the quantity in the parenthesis in equation (49):

$$2\alpha - \beta - \Delta > \alpha - \beta = \phi(1 - \cos\theta_E) > 0. \tag{51}$$

4 Discussion

In this paper, we have neglected some physical features which could be potentially important.

1) In recent experiments [29], the transition is brought about via evaporation of the drop. As the drop evaporates, the Laplace pressure inside the drop increases. It is indicated that this pressure increase can induce the transition. Since the present calculation does not include this effect of volume change of the drop, direct comparison would require a special care. However, the transition itself takes place within a submillisecond (in which duration evaporation could be neglected) in evaporating experiments so that the transition itself could be well described even with neglecting the volume change; although we have to be careful when we compare our quasi-static results with dynamical transitions, it gives some insight; our result could be compared fairly well with evaporation experiments (or experiments in which a transition is initiated by *vibration*), in particular when we place some *defect at the center of the contact circle* to initiate a nucleation from the center.

2) The contact angle hysteresis due to the pinning of the contact line at the singular or sharp corner of the top surface of the pillars is important as discussed in [27], which is neglected in the present work. In contrast, the intrinsic hysteresis effect considered in this paper and in [24] is neglected in [27] so that these two sets of works are complementary to each other. We may need a separate paper to develop a theory which includes both the pinning and intrinsic effects of contact angle hysteresis on the basis of the two sets of works.

3) The penetration of the film of pillar thickness in the sunny-side-up phase involves hydrodynamic effects. Recently, this hydrodynamics itself is clearly understood in [18]; we observe penetration of film into the texture on the surface *not from a yolk of the drop but from a liquid bath* and established the Washburn law [28] (*i.e.*, the penetration length is proportional to the square root of the penetration time) in the case of textured surfaces with dependence on texture parameters (*i.e.*, radius, height, and inter-distance of pillars) clarified. Although our quasi-static treatment suggests the physical essence why the yolk (*i.e.* the central) part of the "sunny-side up" is distinguished from "egg white" film (*i.e.* the surrounding doughnut film), we hope to include the dynamical effect in the future work.

5 Conclusion

We consider the transition of a drop on the textured substrates from the Cassie state to the Wenzel state, assuming that nucleation occurs from the center of the bottom of the drop. We derive an expression, equation (19), for intermediate energies applicable both in hydrophilic and hydrophobic cases. Based on this expression, we investigate, in particular in hydrophilic cases, the energy for the process from the Cassie state to Wenzel/sunny-side-up state including CAH. An approximate formula for the intermediate energy is given in equation (37), which is correct for large X.

The scenario clarified by the numerically calculated energy landscape is as follows. Starting from the Cassie state, the nucleus size x expands without changing the macroscopic shape of the drop (X and θ constant), and the nucleus spreads until the size x catches up with the contact circle $X = X_C$. Then, the "nucleus" size x increases simultaneously with the radius of the contact circle X (x and X expands with $x = X$). When the radius X, equal to x, reaches a certain size, there are two possibilities:

- It gets trapped in a (pseudo-) Wenzel state with the final radius X_{PW} both *in the weak penetration regime* ($0 < \alpha < \Delta$) and *in the non-penetration regime* ($\alpha < 0$)
- It goes into the sunny-side-up state for the egg white film of thickness h to grow with the yolk radius X gradually increasing from X_{PW} to the final size X^*_{PW} *in the strong penetration regime* ($\alpha > \Delta$).

We provide expressions to be compared with experiments indicated in [18]:

- The final radius in the (pseudo-) Wenzel state in both regimes of weak penetration ($0 < \alpha < \Delta$) and of non-penetration ($\alpha < 0$) is given in equation (50), which predicts that the final radius gets smaller as CAH becomes larger.
- The initial yolk radius X_{PW} for $\alpha > \Delta$ is given in equation (49), which asserts that the initial size increases with the CAH.
- The final yolk size X^*_{PW} in the sunny-side-up state for $\alpha > \Delta$ is given in equation (35) or in its good approximation equation (36). This size is independent of the CAH and is simply given as the radius when the contact angle is $\overline{\theta}_C$ given in equation (18), *i.e.*, the average of the contact angle on the solid and the "liquid" substrates.

We need to measure δ to compare some of these equations with experiments. In reality, δ in equations (30) and (31) are different; in such a case Δ is given as $\Delta = (r-1)\delta_p + (1-\phi)\delta_b$.

The authors are grateful to David Quéré and Mathilde Reyssat for discussions. K.O. deeply thanks Halim Kusumaatmajya in Julia Yeomans' group for thoughtful comments on the draft of our paper. This work is supported by research grants, SAKURA (JSPS) and KAKENHI (MEXT, Japan).

References

1. C. Neinhuis, W. Barthlott, Ann. Bot. **79**, 667 (1997).
2. T. Onda, S. Shibuichi, N. Satoh, K. Tsujii, Langmuir **12**, 2125 (1996).
3. A. Hozumi, O. Takai, Thin Solid Films **303**, 222 (1997); K. Teshima, H. Sugimura, Y. Inoue, O. Takai, A. Takano, Langmuir **19**, 10624 (2003).

4. P.S. Swain, R. Lipowsky, Langmuir **14**, 6772 (1998); R. Seemann, M. Brinkmann, E.J. Kramer, F.F. Lange, R. Lipowsky, Proc. Natl. Acad. Sci. U.S.A. **102**, 1848 (2005).
5. J. Bico, C. Marzolin, D. Quéré, Europhys. Lett. **47**, 220 (1999); A. Lafuma, D. Quéré, Nat. Mater. **2**, 457 (2003); M. Callies, D. Quéré, Soft Matter **1**, 55 (2005).
6. K. Okumura, F. Chevy, D. Richard, D. Quéré, C. Clanet, Europhys. Lett. **62**, 237 (2003).
7. S. Herminghaus, Europhys. Lett. **52**, 165 (2000); A. Otten, S. Herminghaus, Langmuir **20**, 2405 (2004).
8. D. Öner, T.J. McCarthy, Langmuir **16**, 7777 (2000).
9. M. Miwa, A. Nakajima, A. Fujishima, K. Hashimoto, T. Watanabe, Langmuir **16**, 5754 (2000); Z. Yoshimitsu, A. Nakajima, T. Watanabe, K. Hashimoto, Langmuir **18**, 5818 (2002).
10. N.A. Patanker, Langmuir **19**, 1249 (2003); **20**, 7097 (2004); **20**, 8209 (2004); B. He, N.A. Patanker, J. Lee, Langmuir **19**, 4999 (2003).
11. A. Marmur, Langmuir **19**, 8343 (2003); **20**, 3517 (2004).
12. R. Narhe, D. Beysens, Phys. Rev. Lett. **93**, 076103 (2004); Europhys. Lett. **75**, 98 (2006).
13. A. Dupuis, J.M. Yeomans, Langmuir **21**, 2624 (2005); Europhys. Lett. **75**, 105 (2006); H. Kusumaatmaja, J. Léopoldès, A. Dupuis, J.M. Yeomans, Europhys. Lett. **73**, 740 (2006).
14. X. Wu, L. Zheng, D. Wu, Langmuir **21**, 2665 (2005).
15. J. Léopoldès, D.G. Bucknall, Europhys. Lett. **72**, 597 (2005).
16. S. Singh, J. Houston, F. van Swol, C.J. Brinker, Nature **442**, 526 (2006).
17. R. Daw, Nature **436**, 471 (2005); M. Jin *et al.*, Adv. Mater. **17**, 1977 (2005); C. Journet, S. Moulinet, C. Ybert, S.T. Purcell, L. Bocquet, Europhys. Lett. **71**, 104 (2005).
18. C. Ishino, M. Reyssat, E. Reyssat, K. Okumura, D. Quéré, Europhys. Lett. **79**, 56005 (2007).
19. D. Bartolo, F. Bouamrirene, É. Verneuil, A. Buguin, P. Silberzan, S. Moulinet, Europhys. Lett. **74**, 299 (2006); M. Reyssat, A. Pépin, F. Marty, Y. Chen, D. Quéré, Europhys. Lett. **74**, 306 (2006).
20. L. Courbin, E. Denieul, E. Dressaire, M. Roper, A. Ajdari, H.A. Stone, Nature Mater. **6**, 661 (2007).
21. S. Diertrich, M.N. Popescu, M. Rauscher, J. Phys.: Condens. Matter **17**, S577 (2005).
22. M. Tasinkevych, S. Dietrich, Phys. Rev. Lett. **97**, 106102 (2006).
23. C. Ishino, K. Okumura, D. Quéré, Europhys. Lett. **68**, 419 (2004).
24. C. Ishino, K. Okumura, Europhys. Lett. **76**, 464 (2006).
25. S. Moulinet, D. Bartolo, Eur. Phys. J. E **24**, 251 (2007).
26. A. de Simon, N. Grunewaldy, F. Otto, *A New Model for Contact Angle Hysteresis*, preprint.
27. H. Kusumaatmajya, J.M. Yeomans, Langmuir **23**, 6019 (2007); H. Kusumaatmajya, M.L. Blow, A. Dupuis; J.M. Yeomans, Europhys. Lett. **81**, 36003 (2008).
28. P.G. De Gennes, F. Brochard-Wyart, D. Quéré, *Gouttes, Bulles, Perles et Ondes* (Belin, Paris, 2002).
29. M. Reyssat, J.M. Yeomans, D. Quéré, Europhys. Lett. **81**, 26006 (2008).